

Physical origin of current partition at a topological trifurcation

Sanyi You, Tao Hou , Zhengtian Li, and Zhenhua Qiao *

*ICQD, Hefei National Research Center for Physical Sciences at the Microscale,
CAS Key Laboratory of Strongly-Coupled Quantum Matter Physics, and Department of Physics,
University of Science and Technology of China, Hefei, Anhui 230026, China*

 (Received 17 April 2021; revised 4 October 2022; accepted 14 October 2022; published 28 October 2022)

In gated bilayer graphene, topological zero-line modes (ZLMs) appear along lines separating regions with opposite valley Hall topologies. Although it is experimentally difficult to design the electric gates to realize ZLMs due to the extremely challenging techniques, twisted bilayer graphene provides a natural platform to produce ZLMs in the presence of a uniform electric field. In this Letter, we develop a set of wave-packet dynamics for ZLMs in monolayer graphene, which can be utilized to characterize various gapless edge modes and can quantitatively reproduce the electronic transport properties at topological intersections. To our surprise, at a topological trifurcation, we show that the counterintuitive current partition (i.e., the direct transport propagation) originates from the microscopic mechanism “bypass jump” which is proved to exist in both monolayer and bilayer systems. Our method can be applied to understand the microscopic pictures of the electronic transport features of all kinds of topological states.

DOI: [10.1103/PhysRevB.106.L161413](https://doi.org/10.1103/PhysRevB.106.L161413)

Introduction. Topological zero-line modes (ZLMs) can arise at interfaces separating different topological systems, e.g., classical wave systems [1–7], non-Hermitian systems [8,9], and various graphene systems [10–33]. Because of their robustness against backscattering, ZLMs have attracted much attention in designing low-power topological quantum devices. In particular, gated AB-stacked bilayer graphene acts as an ideal platform in generating the ZLMs along zero-field lines separating the regions with opposite valley Hall topologies. However, the requirements of extremely precise alignment of the electric gates in bilayer graphene made it unrealistic for large-scale industrial application. Fortunately, the manipulation of “twisting” made bilayer graphene again the central focus in both theoretical and experimental condensed-matter physics. The twisted bilayer graphene and other van der Waals materials then naturally provide ideal platforms (i.e., metallic moiré pattern networks) in designing ZLMs in the presence of a uniform electric field [34–40] or a substrate effect [41].

So far, although there has been great progress in exploring the electronic transport properties of the ZLMs from both numerical calculations and experiments from a macro perspective, it is still analytically unsolvable whenever the zero line becomes curved or crossing. The reason is that it is extremely challenging to derive the analytical solution of the two-dimensional Dirac equation for curved ZLMs or arbitrary topological ZLM intersections [27]. Therefore, the fundamental physical understanding of the transport characteristics of ZLMs is still missing.

Time-dependent Schrödinger equations and wave-packet dynamics provide powerful tools in investigating the motion and scattering problems of quantum particles from an intuitive

and time-dependent perspective. In several low-dimensional materials, the wave-packet propagations have been investigated [42–46], but only the evolution of a simple Gaussian wave packet is adopted in most cases [43–46]. However, the Gaussian wave packet is not the eigenstate of the Hamiltonian of the topological system, but leads to strong dissipation during the evolution.

In this Letter, we develop a set of wave-packet dynamics for ZLMs in monolayer graphene, which can clearly describe the time-dependent evolution of the ZLM at topological intersections. By tracking the trajectories of the electron wave packets at various topological intersections, one can obtain the corresponding current partition ratios in an intuitive manner. In particular, unlike topological bifurcation where forward scattering is forbidden, in a topological trifurcation, based on a simplified but effective monolayer graphene model, we find that the incoming wave packet is divided into three parts at the intersection, where the direct transmission tunneling is not so “direct” along the trifurcation point but originates from the “bypass jump” scattering mechanism which is also proved to exist in gated Bernal bilayer graphene. Our proposed method provides a powerful tool in revealing the time-dependent trajectories of electrons and judging the transport properties in topological materials.

Time-evolution operator. To numerically investigate the electronic properties of ZLMs, the π -orbital tight-binding model Hamiltonian of monolayer graphene with sublattice potentials is adopted to obtain all of our wave-packet dynamics results as follows:

$$H = -\gamma \sum_{\langle ij \rangle} c_i^\dagger c_j + \sum_{i \in A} U_A c_i^\dagger c_i + \sum_{i \in B} U_B c_i^\dagger c_i, \quad (1)$$

where c_i^\dagger (c_i) is a creation (annihilation) operator for an electron at site i , and $\gamma = 2.7$ eV is the nearest-neighbor hopping

*Corresponding author: qiao@ustc.edu.cn

energy. U_A and U_B are the staggered AB sublattice site potentials, satisfying $U_A = -U_B = \lambda\gamma$. We set $\lambda = 0.05$ in Fig. 2, and $\lambda = 0.08$ in Figs. 3 and 4.

Based on the time-evolution operator,

$$\Psi(x, y, t + \Delta t) = \exp\left(-\frac{i}{\hbar}H\Delta t\right)\Psi(x, y, t). \quad (2)$$

By applying the Cayley form to facilitate matrix operation [47], we have

$$\left(1 + \frac{i}{2\hbar}H\Delta t\right)\Psi(x, y, t + \Delta t) \approx \left(1 - \frac{i}{2\hbar}H\Delta t\right)\Psi(x, y, t). \quad (3)$$

If the initial wave function $\Psi(x, y, t)$ is known, the propagated wave function at each time step Δt can be obtained. In Ref. [48], the split-operator technique [43,44] is used to perform matrix operations more efficiently.

Initial wave function. Constructing a proper initial wave function is essential in the time-evolution problem. After Fourier transform, the corresponding low-energy continuum Hamiltonian near the Dirac points with a position-dependent Dirac mass can be expressed as $h = v_F(\tau_z\sigma_x\hat{p}_x + \sigma_y\hat{p}_y) + \sigma_zm(x, y)$, where v_F is the Fermi velocity and $\tau_z = \pm 1$ labels valleys K and K' . Let us focus on the simplest zero-line case along the y axis for the specific K point, i.e., $m(x, y) = m\text{sgn}(x)$, with m being a constant. By solving the time-independent Dirac equation $h\Psi = E\Psi$, one obtains that, when $|E| \geq |m|$, the eigenspinors are extended states, and when $|E| < |m|$, the eigenspinors can be written as

$$\Psi_x = \exp\left(\frac{-|m||x| + i\text{sgn}(m)Ey}{\hbar v_F}\right) \begin{bmatrix} 1 - i\text{sgn}(m) \\ 1 + i\text{sgn}(m) \end{bmatrix}. \quad (4)$$

Similarly, when the zero line is along the x direction, i.e., $m(x, y) = m\text{sgn}(y)$, the eigenspinors for $|E| < |m|$ are

$$\Psi_y = \exp\left(\frac{-|m||y| - i\text{sgn}(m)Ex}{\hbar v_F}\right) \begin{bmatrix} 1 \\ -\text{sgn}(m) \end{bmatrix}. \quad (5)$$

The width d in the direction normal to the zero line is proportional to $1/m(x, y)$. For $|E| < |m|$, based on the linear dispersion of $E = \hbar v_F k$, Eq. (5) can be rewritten as

$$\Psi_y = \exp\left(-\frac{|y|}{d}\right) \exp[-i\text{sgn}(m)kx] \begin{bmatrix} 1 \\ -\text{sgn}(m) \end{bmatrix}, \quad (6)$$

which implies that ZLM is a plane wave in the propagation direction, but becomes localized within a limited transverse direction. To construct a wave packet at certain moment t , one can introduce a Gaussian term in the propagation direction. When setting the wave-packet center to be $\vec{r}_0 = (x_0, y_0)$ in real space and k_0 in reciprocal space, it is noteworthy that Eq. (6) only applies to the zero-line mode of the zigzag boundary, while the zigzag boundary of our studied sample [see Fig. 1(a)] is along the y direction, so Eq. (6) can be expressed as follows:

$$\Psi(x, y) = N \exp\left(-\frac{|x - x_0|}{d_1} - \frac{(y - y_0)^2}{2d_2^2}\right) \exp(ik_0y) \begin{bmatrix} 1 \\ 1 \end{bmatrix}, \quad (7)$$

where $m < 0$, N is the normalization factor, $d_1 = \hbar v_F/|m|$, and $d_2 = \hbar v_F/\Delta E$. Within the tight-binding model [Eq. (1)], we consider the initial wave packet as a discrete form of

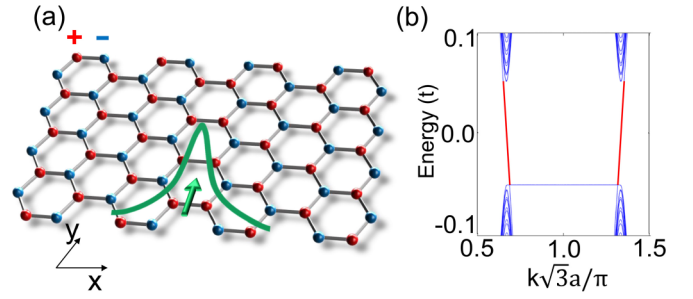


FIG. 1. (a) Schematic plot of a single straight zero line in monolayer graphene. Red and blue denote “+/-” sublattice potentials, respectively. (b) Band structures for the zero line in monolayer zigzag nanoribbon.

Eq. (7) for the graphene hexagonal lattice, the wave function is only distributed on each carbon atom, and we take $k_0 = 4\sqrt{3}\pi/9a$ at the K point [see Fig. 1(b)], with a being the lattice constant of graphene; i.e., the mean energy of the wave packet is zero.

Wave-packet dynamics at bifurcation point. Let us first examine the wave-packet dynamics at a bifurcation point. $\langle r \rangle$ measures the distance between the wave-packet center and the coordinate origin [i.e., topological intersection] and is defined as $\langle r \rangle = \sqrt{\langle x \rangle^2 + \langle y \rangle^2}$, with $\langle x(y) \rangle = \langle \Psi|x(y)|\Psi \rangle$. As shown in Fig. 2(a), in the straight zero line, the wave packet keeps moving forward along the zero line without any backscattering; i.e., $\langle r \rangle$ versus time is almost linear. For the right-angled zero line [see Fig. 2(b)], the wave packet from the bottom has a probability of over 99% of turning into the left zero line, exhibiting a zero bending resistance [15] of ZLM. One can see that the minimum of $\langle r \rangle$ is nonzero, meaning that the wave

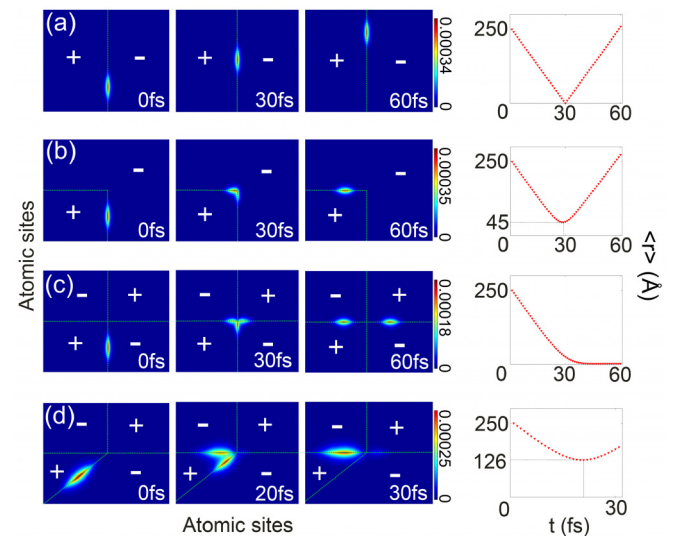


FIG. 2. Time evolution of the wave packet and $\langle r \rangle$ for (a) a single straight zero line, (b) a right-angled zero line, (c) crisscross zero lines, and (d) a bifurcation with a 30° sharp angle. The sample sizes are $L = 170.3$ nm and $W = 98.4$ nm in panels (a)–(c) and $L = 97.0$ nm and $W = 56.1$ nm in panel (d). $d_1 = 4.2$ nm, $d_2 = 10.0$ nm. $\langle r_0 \rangle = 25.0$ nm. The + and – signs indicate the alternating sublattice potentials.

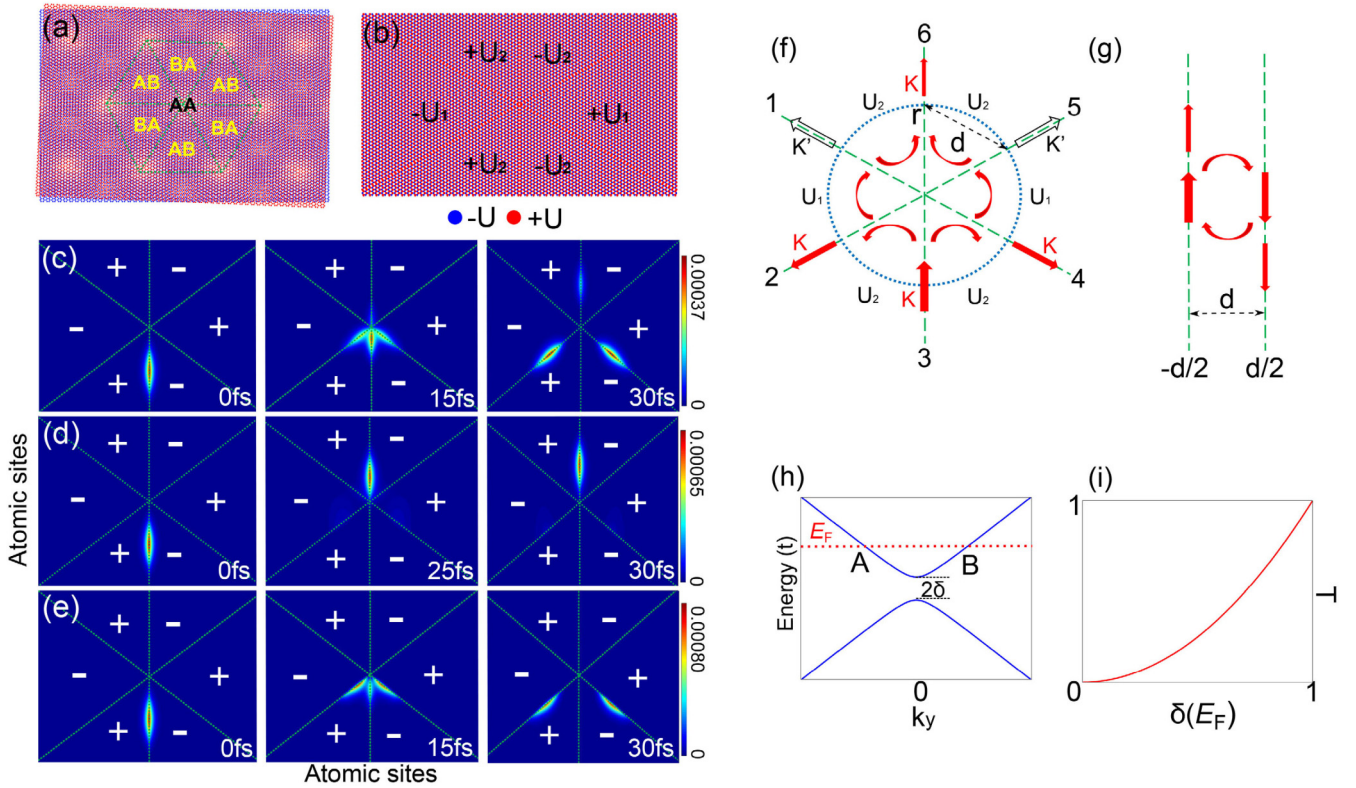


FIG. 3. (a) Schematic view of twisted bilayer graphene. The AA (in black) regions denote the topological intersection. The green lines denote the topological zero lines that separate alternating AB and BA regions distinguished by different valley Chern numbers. (b) Corresponding simulation of topological intersection in monolayer graphene with sublattice-staggered potentials labeled in blue and red. (c)–(e) Time evolution of the wave packet. We have $U_1 = U_2 = \lambda\gamma$ in panel (c), $U_1 = 0.1U_2 = 0.1\lambda\gamma$ in panel (d), and $U_1 = 4U_2 = 4\lambda\gamma$ in panel (e), where $\lambda = 0.08$. The sample sizes are $L = 97.4$ nm and $W = 56.8$ nm in panels (c)–(e). $d_1 = 2.6$ nm, $d_2 = 6.0$ nm. $\langle r_0 \rangle = 14.0$ nm. The + and – signs indicate the alternating sublattice potentials. (f) Simplified schematic of Fig. 3(b), the red and black arrows represent the permitted and the not permitted scattering direction of the electron wave packet. (g) At a circumference with a given r , a sketch of the tunneling between adjacent topological zero lines with a distance of d is shown. (h) Low-energy spectrum near valley K of the two topological zero lines illustrated in panel (g) with a gap induced by the finite-size effect. The red dashed line indicates the Fermi level. (i) Scattering rate versus gap δ .

packet never reaches the exact turning point during the propagation. In Fig. 2(c), the wave packet is equally partitioned into two parts at the bifurcation point. Figure 2(d) shows the propagation of the wave packet at a sharp turn, where the probability of turning to the left is around 91% and the rest turn to right. This indicates that, the shorter the distance between the incoming channel and the scattering channel, the easier it is for the scattering between the channels to occur. All these observations and the magnetic field effect of our wave-packet dynamics in Ref. [48] are exactly consistent with the findings from electronic transport by using Green’s function technique [13,15,16], strongly suggesting the feasibility of our wave-packet dynamics in investigating the fundamental properties of ZLMs.

Origin of unusual electronic transport at trifurcation point. Minimally twisted bilayer graphene provides a natural system in designing ZLM-based electronics [49–53]. However, the physical origin of the current partition at the trifurcation point is still unclear; e.g., how can part of the incoming current directly pass through the trifurcation point? Moreover, the number of atoms in a unit cell at a tiny twist angle is extremely large and therefore the numerical calculation is extremely

time-consuming or out of the computational capability. Considering that gated AB-stacked bilayer graphene and gated minimally twisted bilayer graphene are equivalent in the scattering problem of trifurcation, for the study of the bilayer system, we choose the gated AB-stacked bilayer graphene as our research object, in which the number of atoms is greatly reduced.

First, for clarity, we apply the developed wave-packet dynamics in the monolayer graphene model as displayed in Fig. 3(b) with the conducting topological channels highlighted. For the ZLM encoded with certain valley K [e.g., incoming from terminal 3], the permitted outgoing terminals are terminals 2, 4, and 6. In twisted bilayer graphene [see Fig. 3(a)], the AA-stacked region shrinks with decreasing twisted angle. Unless otherwise specified, in all simulations of monolayer graphene, the zero-line width (corresponding to the AA region in twisted bilayer graphene) is set to be the same as a single hexagonal lattice. When we set $U_1 = U_2 = \lambda\gamma$, the electron wave packet from terminal 3 is partitioned into three parts into terminals 2, 4, and 6 at the topological intersection [see Fig. 3(c)]. Although the central metallic area is limited enough, the squared modulus of the

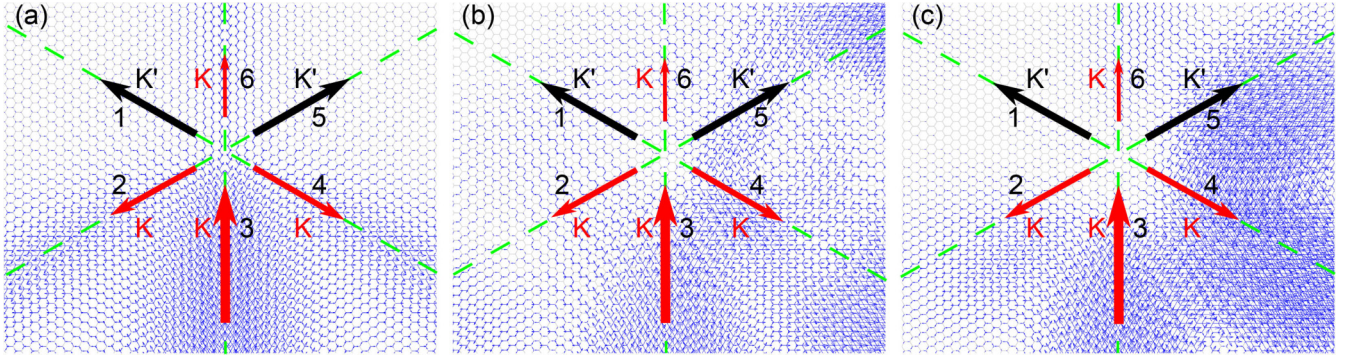


FIG. 4. (a)–(c) Current densities of topological trifurcations in monolayer graphene with staggered sublattice potentials and Bernal bilayer graphene with patterned interlayer bias at a Fermi level energy of 0.0027 eV. Panel (a) is the monolayer system, and panels (b) and (c) are the bottom layer and the top layer of the bilayer system, respectively. The green dashed lines are topological zero lines, and the numbers 1–6 are terminals corresponding to the settings in Fig. 3(f).

forward-propagating wave packet into terminal 6 is approximately 14%, agreeing well with the result from the Landauer-Büttiker formalism [52], and the rest is equally partitioned towards adjacent terminals 2 and 4. The partition to the adjacent zero lines is well understood due to the overlap between the incoming and outgoing wave functions [16]. Previously, we attributed the forward propagation to the contribution of the narrow graphene ribbon with the same site-potential (corresponding to the AA-stacked ribbon with uniform bias in twisted bilayer graphene). However, this is not true. Hereinbelow, we provide an analytical understanding by using the developed wave-packet dynamics and effective models.

In Fig. 2(b), one can observe that the current never reaches the turning point when there is an angle between incoming and outgoing zero lines. To clarify, we construct an effective model of coupled zero lines. At a circumference with a given radius r of Fig. 3(f), the local electronic structure of the six intersection points between the circle with a given r and the trifurcation can be approximated by antiparallel topological zero lines with a distance d [see Fig. 3(g)]. We attribute the interaction strength δ between zero-line modes to their mixing in the overlapping region of wave functions [54], i.e.,

$$\delta = \frac{|U|}{d} \int_{-d/2}^{d/2} \psi(x)_{-d/2}^* \psi(x)_{d/2} dx = |U| \exp\left[-\frac{|U|d}{\hbar v_F}\right], \quad (8)$$

where

$$\psi_{\pm d/2} = \exp\left[\pm \frac{|U|}{\hbar v_F}(x \mp d/2)\right]. \quad (9)$$

One can get the solution of K' from that of K by setting \hat{p} to be $-\hat{p}$. So we only need to focus on K in the following. The effective Hamiltonian of antiparallel zero lines at K can be written as

$$H(k_y) = \begin{bmatrix} \hbar v_F k_y & \delta \\ \delta & -\hbar v_F k_y \end{bmatrix}, \quad (10)$$

where the diagonal elements describe the counterpropagating ZLMs encoded with valley K . The energy dispersions and

wave functions are respectively

$$E_{\pm} = \pm \sqrt{(\hbar v_F k_y)^2 + \delta^2}, \quad (11)$$

$$\Psi_{\pm} = \frac{\exp(ik_y y)}{\sqrt{(E_{\pm} + \hbar v_F k_y)^2 + \delta^2}} \begin{bmatrix} E_{\pm} + \hbar v_F k_y \\ \delta \end{bmatrix}. \quad (12)$$

The low-energy spectrum is displayed in Fig. 3(h). The scattering rate between adjacent channels [e.g., between states A and B at the same energy] can be given by

$$T = |\langle \Psi_+(-k_y) | \Psi_+(+k_y) \rangle|^2 = (\delta/E_+)^2, \quad (13)$$

which is displayed in Fig. 3(i). When the gap induced by the interaction is vanishing, it means that the electron is located at infinity where there is no coupling between adjacent channels, and thus the scattering rate is zero. As the electron approaches the intersection, δ increases and the electron becomes scattered to the outgoing zero line. The Fermi energy of the electron determines its closest distance to the intersection.

Next, we extend the effective model to six interacting counterpropagating zero-line modes encoded with valley K at the same circumference [see Fig. 3(f)]. The corresponding Hamiltonian is

$$\begin{bmatrix} \hbar v_F k_y & \delta & 0 & 0 & 0 & \delta \\ \delta & -\hbar v_F k_y & \delta & 0 & 0 & 0 \\ 0 & \delta & \hbar v_F k_y & \delta & 0 & 0 \\ 0 & 0 & \delta & -\hbar v_F k_y & \delta & 0 \\ 0 & 0 & 0 & \delta & \hbar v_F k_y & \delta \\ \delta & 0 & 0 & 0 & \delta & -\hbar v_F k_y \end{bmatrix}, \quad (14)$$

and the dispersion relations are

$$E_{1\pm} = \pm \sqrt{(\hbar v_F k_y)^2 + \delta^2}, \quad (15)$$

$$E_{2\pm} = \pm \sqrt{(\hbar v_F k_y)^2 + 4\delta^2}, \quad (16)$$

where $E_{1\pm}$ are doubly degenerate. As the radius of the circumference decreases, the energy gap of the system becomes larger. Therefore, there is no low-energy electronic state near the trifurcation point; i.e., theoretically no electron at low energy can reach the intersection. However, why is there still forward propagation of the electronic transport?

To show the scattering process intuitively, one can consider a scattering model as displayed in Fig. 3(f). According to Eq. (13), let us assume an incoming electron [encoded with valley K] from terminal 3. It can be scattered into outgoing terminals 2 and 4. It is naturally expected that the outgoing current at terminal 2(4) can also be scattering into incoming terminals 1(5) and 3. And subsequently, the incoming current at terminal 1(5) can further be scattered into outgoing terminals 6 and 2(4). This indicates that the “direct” transmitting current from terminal 3 to terminal 6 is not so “direct,” but undergoes a complex route along the paths of $3 \Rightarrow 2(4) \Rightarrow 1(5) \Rightarrow 6$. In a recent work [52], the clue of the “bypass jump” can be inferred from the fact that forward scattering is insensitive to the increasing size of the narrow graphene ribbon with the same site-potential within a certain range. We also construct effective models of gated Bernal bilayer graphene [48], and the results show that the scattering mechanism of the “bypass jump” is still valid.

The more direct evidence of the existence of the “bypass jump” mechanism is that we obtained the current densities of the topological trifurcations in monolayer and bilayer systems based on the nonequilibrium Green’s function method [48], which intuitively display the current flow. In Fig. 4, the size and direction of the blue arrows indicate the magnitude and flow direction of the current, respectively. In the monolayer system, i.e., Fig. 4(a), current from terminal 3 to terminal 6 undergoes a complex route along the paths of $3 \Rightarrow 2(4) \Rightarrow 1(5) \Rightarrow 6$. Interestingly, in the bottom layer [Fig. 4(b)] and the top layer [Fig. 4(c)] of biased Bernal bilayer graphene, the area where current is forbidden to pass is larger near the topological trifurcation, and the process of scattering via terminal 5 into terminals 4 and 6 is clearly shown.

Based on the above analysis, a topological transistor for the monolayer system can be designed by tuning the ratio of U_1/U_2 to realize the on-off state [see Fig. 5(c)]; i.e., the scattering probability T_{63} from terminal 3 to terminal 6 can be continuously tuned between 0 and 1. In particular, when $U_1/U_2 = 0.1$, $T_{63} = 0.83$ [see Fig. 3(d)]; when $U_1/U_2 = 4.0$, $T_{63} = 0$ [see Fig. 3(e)]. In Figs. 5(a) and 5(b), one can clearly observe the direct coupling of wave functions between adjacent channels [e.g., 1 and 2] when $U_1/U_2 = 0.1$. On the contrary, the penetration depth of the electron wave packet in the U_1 regions approaches zero and the scattering by “bypass jump” becomes vanishing when $U_1/U_2 = 4.0$. In Ref. [48], we demonstrate how to manipulating T_{63} via tuning the ratio of U_1/U_2 . Interestingly, the design of the topological transistor also implies the “bypass jump” mechanism of electrons, because increasing the sublattice potentials of the U_1 region [i.e., decreasing the gap δ of the U_1 region in Fig. 5(d)] is

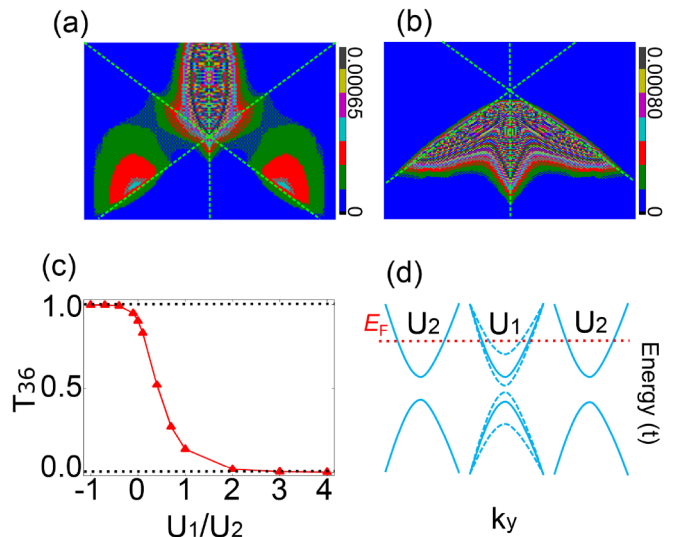


FIG. 5. (a) and (b) Zoom of the second subgraph of Figs. 3(d) and 3(e). (c) Scattering rate from terminal 3 to terminal 6 versus the ratio of U_1/U_2 . (d) At a circumference with a given r , the evolution of the band structure from terminal 3 to terminal 6 is shown.

equivalent to cutting off the propagation path of the electron wave packet.

Conclusion. In summary, we demonstrate the zero bending resistance and the ballistic transport properties at a sharp turn from a microscopic point of view. At the topological trifurcation point belonging to the monolayer system, an alternative current partition rule modulated by the relations between U_1 and U_2 is clarified. In particular, in both monolayer and bilayer systems, an alternative scattering mechanism in the form of a “bypass jump” is revealed to understand the unusual current partition at the topological trifurcation point. Our methods can not only be used to study the electronic transport properties of other topological systems but also open up an alternative avenue to investigate the electronic transport behaviors of electron wave packets in large-scale topological networks.

Acknowledgments. We thank Professors Q. Niu, J. Zeng, and Y. Han for useful discussion. This work was financially supported by the NNSFC (Grant No. 11974327), the Fundamental Research Funds for the Central Universities (Grants No. WK351000010 and No. WK2030020032), and the Anhui Initiative in Quantum Information Technologies. We also thank the supercomputing service of AM-HPC and the Supercomputing Center of University of Science and Technology of China for providing the high-performance computing resources.

[1] J. Lu, C. Qiu, L. Ye, X. Fan, M. Ke, F. Zhang, and Z. Liu, *Nat. Phys.* **13**, 369 (2017).
 [2] M. Yan, J. Lu, F. Li, W. Deng, X. Huang, J. Ma, and Z. Liu, *Nat. Mater.* **17**, 993 (2018).
 [3] J. Lu, C. Qiu, W. Deng, X. Huang, F. Li, F. Zhang, S. Chen, and Z. Liu, *Phys. Rev. Lett.* **120**, 116802 (2018).
 [4] X. Wu, Y. Meng, J. Tian, Y. Huang, H. Xiang, D. Han, and W. Wen, *Nat. Commun.* **8**, 1304 (2017).

[5] J. Dong, X. Chen, H. Zhu, Y. Wang, and X. Zhang, *Nat. Mater.* **16**, 298 (2017).
 [6] J. Noh, S. Huang, K. P. Chen, and M. C. Rechtsman, *Phys. Rev. Lett.* **120**, 063902 (2018).
 [7] S. Zheng, J. Zhang, G. Duan, Z. Jiang, X. Man, D. Yu, and B. Xia, *Phys. Rev. B* **105**, 184104 (2022).
 [8] W. Song, W. Sun, C. Chen, Q. Song, S. Xiao, S. Zhu, and T. Li, *Phys. Rev. Lett.* **123**, 165701 (2019).

- [9] T.-S. Deng and W. Yi, *Phys. Rev. B* **100**, 035102 (2019).
- [10] G. W. Semenoff, V. Semenoff, and F. Zhou, *Phys. Rev. Lett.* **101**, 087204 (2008).
- [11] I. Martin, Y. M. Blanter, and A. F. Morpurgo, *Phys. Rev. Lett.* **100**, 036804 (2008).
- [12] K. Wang, T. Hou, Y. Ren, and Z. Qiao, *Front. Phys.* **14**, 23501 (2019).
- [13] K. Wang, Y. Ren, X. Deng, S. A. Yang, J. Jung, and Z. Qiao, *Phys. Rev. B* **95**, 245420 (2017).
- [14] Y. Ren, J. Zeng, K. Wang, F. Xu, and Z. Qiao, *Phys. Rev. B* **96**, 155445 (2017).
- [15] Z. Qiao, J. Jung, Q. Niu, and A. H. MacDonald, *Nano Lett.* **11**, 3453 (2011).
- [16] Z. Qiao, J. Jung, C. Lin, Y. Ren, A. H. MacDonald, and Q. Niu, *Phys. Rev. Lett.* **112**, 206601 (2014).
- [17] S.-g. Cheng, H. Liu, H. Jiang, Q.-F. Sun, and X. C. Xie, *Phys. Rev. Lett.* **121**, 156801 (2018).
- [18] T. Hou, G. Cheng, W.-K. Tse, C. Zeng, and Z. Qiao, *Phys. Rev. B* **98**, 245417 (2018).
- [19] J. Jung, F. Zhang, Z. Qiao, and A. H. MacDonald, *Phys. Rev. B* **84**, 075418 (2011).
- [20] Y.-T. Zhang, Z. Qiao, and Q.-F. Sun, *Phys. Rev. B* **87**, 235405 (2013).
- [21] X. Bi, J. Jung, and Z. Qiao, *Phys. Rev. B* **92**, 235421 (2015).
- [22] L. Ju, Z. Shi, N. Nair, Y. Lv, C. Jin, J. Velasco, Jr., H. A. Bechtel, M. C. Martin, A. Zettl, J. Analytis, and F. Wang, *Nature (London)* **520**, 650 (2015).
- [23] J. Li, K. Wang, Kenton J. McFaul, Z. Zern, Y. Ren, K. Watanabe, T. Taniguchi, Z. Qiao, and J. Zhu, *Nat. Nanotechnol.* **11**, 1060 (2016).
- [24] J. Li, R. Zhang, Z. Yin, J. Zhang, K. Watanabe, T. Taniguchi, C. Liu, and J. Zhu, *Science* **362**, 1149 (2018).
- [25] H. Pan, X. Li, F. Zhang, and S. A. Yang, *Phys. Rev. B* **92**, 041404(R) (2015).
- [26] M. Wang, L. Liu, C.-C. Liu, and Y. Yao, *Phys. Rev. B* **93**, 155412 (2016).
- [27] J. R. Anglin and A. Schulz, *Phys. Rev. B* **95**, 045430 (2017).
- [28] C. Lee, G. Kim, J. Jung, and H. Min, *Phys. Rev. B* **94**, 125438 (2016).
- [29] M. Kim, J. H. Choi, S. H. Lee, K. Watanabe, T. Taniguchi, S. H. Jhi, and H. J. Lee, *Nat. Phys.* **12**, 1022 (2016).
- [30] D. Xiao, W. Yao, and Q. Niu, *Phys. Rev. Lett.* **99**, 236809 (2007).
- [31] F. Zhang, A. H. MacDonald, and E. J. Mele, *Proc. Natl. Acad. Sci. USA* **110**, 10546 (2013).
- [32] Z. Yan, T. Hou, Y. Han, X. Xu, and Z. Qiao, *Phys. Rev. B* **105**, 035425 (2022).
- [33] Y. Han, S. You, and Z. Qiao, *Phys. Rev. B* **105**, 155301 (2022).
- [34] S. Huang, K. Kim, D. K. Efimkin, T. Lovorn, T. Taniguchi, K. Watanabe, A. H. MacDonald, E. Tutuc, and B. J. LeRoy, *Phys. Rev. Lett.* **121**, 037702 (2018).
- [35] P. Rickhaus, J. Wallbank, S. Slizovskiy, R. Pisoni, H. Overweg, Y. Lee, M. Eich, M. Liu, K. Watanabe, T. Taniguchi, V. Fal'ko, T. Ihn, and K. Ensslin, *Nano Lett.* **18**, 6725 (2018).
- [36] S. S. Sunku, G. Ni, B. Jiang, H. Yoo, A. Sternbach, A. S. McLeod, T. Stauber, L. Xiong, T. Taniguchi, K. Watanabe, P. Kim, M. M. Fogler, and D. N. Basov, *Science* **362**, 1153 (2018).
- [37] S. Xu, A. I. Berdyugin, P. Kumaravadivel, F. Guinea, R. Krishna Kumar, D. A. Bandurin, S. V. Morozov, W. Kuang, B. Tsim, S. Liu, J. H. Edgar, I. V. Grigorieva, V. I. Fal'ko, M. Kim, and A. K. Geim, *Nat. Commun.* **10**, 4008 (2019).
- [38] H. Yoo, R. Engelke, S. Carr, S. Fang, K. Zhang, P. Cazeaux, S. H. Sung, R. Hovden, A. W. Tsen, T. Taniguchi, K. Watanabe, G. Yi, M. Kim, M. Luskun, E. B. Tadmor, E. Kaxiras, and P. Kim, *Nat. Mater.* **18**, 448 (2019).
- [39] Y.-W. Liu, Y. Su, X.-F. Zhou, L.-J. Yin, C. Yan, S.-Y. Li, W. Yan, S. Han, Z.-Q. Fu, Y. Zhang, Q. Yang, Y.-N. Ren, and L. He, *Phys. Rev. Lett.* **125**, 236102 (2020).
- [40] J. D. Verbakel, Q. Yao, K. Sotthewes, and H. J. W. Zandvliet, *Phys. Rev. B* **103**, 165134 (2021).
- [41] C. Mouldsdales, A. Knothe, and V. Fal'ko, *Phys. Rev. B* **105**, L201112 (2022).
- [42] G. M. Maksimova, V. Ya. Demikhovskii, and E. V. Frolova, *Phys. Rev. B* **78**, 235321 (2008).
- [43] A. Chaves, G. A. Farias, F. M. Peeters, and B. Szafran, *Phys. Rev. B* **80**, 125331 (2009).
- [44] A. Chaves, L. Covaci, K. Y. Rakhimov, G. A. Farias, and F. M. Peeters, *Phys. Rev. B* **82**, 205430 (2010).
- [45] K. Y. Rakhimov, A. Chaves, G. A. Farias, and F. M. Peeters, *J. Phys.: Condens. Matter* **23**, 275801 (2011).
- [46] D. R. da Costa, A. Chaves, G. A. Farias, L. Covaci, and F. M. Peeters, *Phys. Rev. B* **86**, 115434 (2012).
- [47] N. Watanabe and M. Tsukada, *Phys. Rev. E* **62**, 2914 (2000).
- [48] See Supplemental Material at <http://link.aps.org/supplemental/10.1103/PhysRevB.106.L161413> for details, which includes Refs. [11,15,55–57].
- [49] N. N. T. Nam and M. Koshino, *Phys. Rev. B* **96**, 075311 (2017).
- [50] B. Tsim, N. N. T. Nam, and M. Koshino, *Phys. Rev. B* **101**, 125409 (2020).
- [51] T. Hou, Y. Ren, Y. Quan, J. Jung, W. Ren, and Z. Qiao, *Phys. Rev. B* **101**, 201403(R) (2020).
- [52] T. Hou, Y. Ren, Y. Quan, J. Jung, W. Ren, and Z. Qiao, *Phys. Rev. B* **102**, 085433 (2020).
- [53] C. De Beule, F. Dominguez, and P. Recher, *Phys. Rev. Lett.* **125**, 096402 (2020).
- [54] M. Ezawa and N. Nagaosa, *Phys. Rev. B* **88**, 121401(R) (2013).
- [55] H. Jiang, L. Wang, Q.-F. Sun, and X. C. Xie, *Phys. Rev. B* **80**, 165316 (2009).
- [56] Y. Zhang, J.-P. Hu, B. A. Bernevig, X. R. Wang, X. C. Xie, and W. M. Liu, *Phys. Rev. B* **78**, 155413 (2008).
- [57] J.-Y. Yan, P. Zhang, B. Sun, H.-Z. Lu, Z. Wang, S. Duan, and X.-G. Zhao, *Phys. Rev. B* **79**, 115403 (2009).